RESEARCH ARTICLE

ADVANCED
SENSOR
RESEARCH
Open Access

www.advsensorres.com

Sustainable Laser-Induced Graphene Electrochemical Sensors from Natural Cork for Sensitive Tyrosine Detection

Eoghan Vaughan, Chiara Santillo, Michele Setti, Cathal Larrigy, Aidan J. Quinn, Gennaro Gentile, Marino Lavorgna, and Daniela Iacopino*

Cork laser induced graphene (cork-LIG) electrochemical sensors are fabricated by direct laser writing of natural cork sheets. Laser writing is performed with a hobbyist visible laser. The obtained cork-LIG structures display graphene-like Raman signatures, high conductivity, and fast electron-transfer rates. After a 10 min electrochemical pretreatment, electrodes are used for detection of Tyrosine (Tyr) in the presence of uric acid, dopamine, ascorbic acid, urea, and glucose. linear detection of tyrosine is achieved in the 5–150 µm range with a limit of detection (LOD) of 3.03 µm. Calibration of dopamine detection is achieved with a LOD of 1.1 µm. Finally, the cork-LIG electrochemical sensors show linear response of Tyr in artificial sweat in the relevant physiological range of 5–250 μм (sensitivity, 1.8×10^{-2} A м$^{-1}$). The LOD is calculated as 3.75 μм. These results open the door to the exploitation of renewable materials such as cork for the development of high-quality, green sensors for the monitoring of health and wellbeing parameters.

1. Introduction

Cork is a renewable, recyclable, natural material derived from the bark of the *Quercus suber L.* tree. Cork is periodically harvested (every 9–12 years), renewing itself without causing any harm to the tree. The chemical composition of cork is different than wood. It possess lower content of cellulose and hemicellulose, a higher content of the aromatic biopolymer lignin, and has a high content of the aliphatic and aromatic biopolymer suberin.[1,2] At the microscopic level, cork displays a morphology with a honeycomb structure characterized by pentagonally- and hexagonally-arranged hollow cells. The cell walls are covered with highly hydrophobic suberin and lignin molecules. The high surface area and hollow structure, as well as its chemical composition, confer cork a unique set of properties, such as lightness, low-density, compressibility, impermeability, high resistance to combustion, and low thermal conductivity.[3,4] As result, cork is used in a wide variety of products ranging from stoppers for wine bottles, seals, and pads in woodwind instruments, thermal and acoustic insulation, activated carbon. Cork has even been applied as a thermal and antivibration shield in spacecraft by both NASA and ESA.[4]

Direct laser writing techniques have recently emerged as suitable methods for the fast and versatile production of graphene-like materials.[5] In this approach, pioneered by Tour et al., a CO_2 laser is used to "write" features on flexible polymers, usually polyimide.[6–8] The writing process leads to the formation of laser induced graphene (LIG), a high surface area, 3D, conductive ($< 20\ \Omega$ sq^{-1}), graphene-like material resulting from the localized high-temperature, high-pressure environment created by the laser. Among the wide range of uses, the high surface area and high density of defects of LIG materials have proven particularly suitable for electrochemical applications.[9–11] Great efforts in the last few years have focused on the development of laser writing processes applicable to biodegradable and naturally sourced materials, alternative to synthetic, fossil fuel derived polymers. By widening the range of laser wavelengths from the IR (10.6 µm) to the visible (450 and 405 nm) and UV (355 nm), several groups have demonstrated production of LIG from paper,[12–14] cardboard,[15] wood,[16] lignin-rich materials,[17] chitosan-based films,[18] cloth and even food (coconut shells and potato peels).[19,20] Remarkably, these green LIG materials have exhibited Raman spectroscopic signatures of graphene-like materials with I_{2D}/I_G ratios > 0.6 and I_D/I_G ratios close to 1, as well as low sheet resistances ($< 50\ \Omega$ sq^{-1}). Successful proof of concept demonstrations of next generation green electronics have been demonstrated, such as glucose electrochemical

E. Vaughan, M. Setti, C. Larrigy, A. J. Quinn, D. Iacopino
Tyndall National Institute
University College Cork
Dyke Parade, Cork T12R5CP, Ireland
E-mail: daniela.iacopino@tyndall.ie
C. Santillo, M. Lavorgna
Institute for Polymers
Composites and Biomaterials
National Research Council of Italy
P.le E. Fermi 1, Portici 80055, Italy
G. Gentile
Institute for Polymers
Composites and Biomaterials
National Research Council of Italy
via Campi Flegrei, 34, Pozzuoli, Naples 80078, Italy

**ADVANCED
SCIENCE NEWS**

www.advancedsciencenews.com

**ADVANCED
SENSOR
RESEARCH**

www.advsensorres.com

sensing,[21] electronic functionalities for paper electronics,[22] wood electronics,[23] and energy harvesting/storage.[24]

Cork is used either as natural cork, as harvested from the tree, or as agglomerated cork, in which pulped cork is reformed into sheets using a binding agent. Carbonization of natural cork at 1000 °C has been shown to result in a polyaromatic carbon material, between graphitic carbon and amorphous carbon. The honeycomb cell structure of cork was maintained after carbonization, which resulted in an ideal structure for use as a high-performance field emitting device.[25] Recently, laser graphitization of natural and agglomerated cork has been demonstrated with IR, UV, and visible low cost hobbyist lasers. For example, Imbrogno et al. used one-step visible laser writing on natural cork stoppers to fabricate cork-LIG supercapacitors, which showed > 11 mF cm^{-2} areal capacitance and only 14% loss over 10 000 charge discharge cycles.[26] Carvalho et al. have used agglomerated and natural cork-LIG as piezoresistive material for the monitoring of human gait in insoles.[27] Agglomerated cork-LIG triboelectric generators were used in combination with polyimide LIG electrodes, which generated open circuit voltages > 3.5 V and peak power > 8 mV.[28]

In this manuscript, we present for the first time the use of natural cork-LIG electrodes as an electrochemical sensing platform. Cork-LIG was fabricated with a one-step laser irradiation process (450 nm) on pristine cork sheets. Following laser conditions optimization, the fabricated cork-LIG displayed low sheet resistance (10 Ω sq^{-1}), a Raman signature of disordered crystalline graphene-like material and high density of sp^2 carbon bonds. Electrode materials with fast electron transfer rates (k^0_{app} = 9×10^{-3} cm s^{-1} for [Fe(CN)$_6$]$^{3-/4-}$) were obtained after an electrochemical activation process. This process, lasting only 10 min, improved the surface quality of cork-LIG by increasing the percentage of C=C bonds and decreasing the percentage of C—O bonds arising from the laser burning process. As result, sensitive detection of Tyr and concomitant detection of Tyr, dopamine (DA) and uric acid (UA) was achieved, with linear responses in the relevant detection range for physiological fluids. These results introduce a novel, eco-friendly, high-sensitivity electrochemical sensor with qualities that enable monitoring of metabolites in the human body.

2. Results and Discussion

2.1. Device Fabrication

Figure 1a shows the schematic of the fabrication of the cork-LIG electrochemical sensor platform. The cork substrate measured 20 × 20 × 2 mm. Two identical cork-LIG electrodes measuring 11 × 1.5 mm, with 1 mm separation, were scribed using a 450 nm laser. These were used as the working and counter electrode. The active area of the working electrode was reduced to ≈2 × 1.5 mm by passivation with an acrylic-based nail varnish. Ag/AgCl ink was applied close to the LIG electrodes for use as a reference electrode. Conductive Ag paint was applied to the electrodes to allow for connection of the device to the potentiostat when placed in the Teflon cell. Photographs of the ready-to-use device and the assembly in the cell are shown in Figure 1b; and Figure S1b (Supporting Information), respectively. Fabrication time with the laser was 44 s per device, and application of the Ag/AgCl and conductive Ag
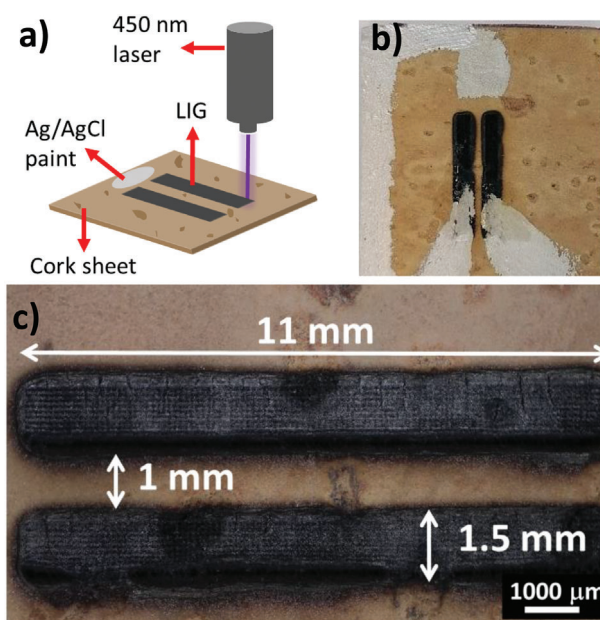

Figure 1. a) Schematic of the laser engraving of the LIG electrodes on cork substrate. b) Photographic image of the planar 3-electrode device on cork. c) White light microscope image of the cork-LIG electrodes.

paint brought the entire fabrication time to ≈10 min for six devices (cork sheets of 40 × 60 mm served for six devices). For the initial optimization of the laser parameters, an external Ag/AgCl reference and a Pt wire counter electrode were used.

2.2. Laser Settings Optimization

LIG electrodes are known for their fast electron transfer rates and high specific surface area, both of which are highly dependent on the laser conditions (wavelength, power, speed).[11,29] While these characteristics have widely been explored for polyimide-LIG, very few examples of cork-LIG are available in literature.[26–28] As such, a detailed investigation of the laser writing process on cork was performed in order to find the optimum conditions for device fabrication. This was done by writing rectangular features (3 × 9 mm) on cork at various laser power/speed (depth adjustment) combinations followed by an investigation of the electrical, Raman, and electrochemical behavior of the cork-LIG.

Figure 2a shows a photograph of the cork-LIG features on cork obtained by using 20–60% laser powers (LP, % of 3 W) and 20–50 depth adjustment (DA) combinations. The resulting cork-LIG structures showed visible differences: at the low end of the scale (low LP, low DA—LP20-DA20) the features appeared dark grey, sharply defined, and were coplanar with the cork substrate. At the high end of the scale (high LP, high DA—LP50-DA50, LP30-DA60) the features appeared black, included a spreading of the graphitized area beyond the desired shape, and were receded into the cork. These structures were classified as surface features and receded features and further analyzed.

Electrical characterization (see Figure 2b) showed that with increasing power, the graphitized features displayed a decreasing sheet resistance—from 54 Ω sq^{-1} at LP30-DA20 to 10 Ω sq^{-1} at LP60-DA30, following a trend already indentified for

ADVANCED
SCIENCE NEWS
www.advancedsciencenews.com

ADVANCED
SENSOR
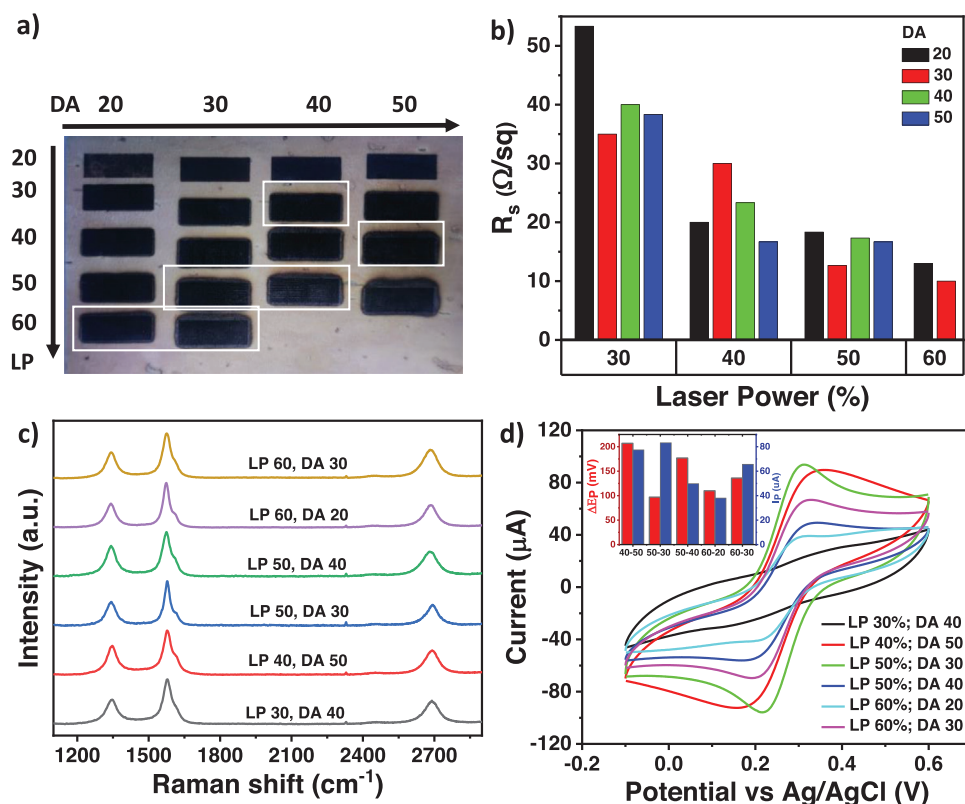**RESEARCH**
Open Access
www.advsensorres.com

Figure 2. a) 3×9 mm features written on cork with varying laser parameters (LP 20 to 60% and DA 20 to 50). b) Sheet resistance measured for cork-LIG structures shown in (a). c) Representative Raman spectra of cork-LIG features shown in (a). d) CV scans (100 mV s^{-1}) of 5 mm Fe[CN]$_6$$^{3-/4-}$ in 1 m KCl at cork-LIG working electrodes obtained under laser settings described in (a). Inset: peak separation and peak current of CVs.

polyimide LIG and also for green LIG derived from biodegradable precursors.[17] Results for LP20% were omitted, as they displayed resistances in the kΩ order of magnitude. Based on these initial findings, cork-LIG samples obtained from six laser settings were selected for further analysis. Representitive Raman spectra for each of the six samples, based on qualities averaged over 15 spectra per sample, are displayed in Figure 2c. The cork-LIG structure obtained at LP30-DA40 represented the surface feature, whereas the cork-LIG structure written at LP60-DA30 represented the extreme of the receeded feature. Despite the visual differences, Raman characterization was not sufficient to discern the quality of one cork-LIG structure over another. Each structure showed distinct and sharp D, G, and 2D peaks. Only small variations of the peaks FWHMs, positions and intensity ratios (I_D/I_G and I_{2D}/I_G) were observed (see full details in Table S1, Supporting Information). The data indicate that high quality LIG was produced at each setting. In order to gain further insight into the most approporiate laser settings for the fabrication of electrode materials, electrochemical characterization of cork-LIG electrodes was carried out using cyclic voltammetry (CV). The standard reversible redox couple Ferro/ferricyanide ([Fe(CN)$_6$]$^{3-/4-}$) was used for this characterization. The peak to peak separation (ΔE_p) and peak current (I_p) were considered as quality selection paramenters. For this optimization step a simple design of a 3 mm wide LIG electrode spanning the 8 mm base of the electrochemical cell was used as working electrode together with external counter (Pt) and reference (Ag/AgCl) electrodes. Figure 2d displays six CV curves

at 100 mV s^{-1} scan rate obtained at the selected laser settings. The cork-LIG produced at LP50-DA30 (green curve) showed the sharpest peaks, with the largest I_p values and the lowest ΔE_p values. The superiority of the LP50-DA30 electrode is clearly evident in the histogram shown as inset in Figure 2d. The full range of data (in triplicates) captured at each setting is shown in Figure S2 (Supporting Information), and confirmed that LP50-DA30 was the optimal setting considering kinetics, current response, and repeatability. All further data presented in this work were obtained with cork-LIG structures fabricated at LP50-DA30.

2.3. Material Characterization

Following selection of the optimal writing conditions, further characterization of the cork-LIG material was carried out.

Scanning electron microscope (SEM) micrographs of the pristine cork surface and the cork-LIG surface are displayed in **Figure 3**. Low (3a) and high (3b) magnification images of raw cork show the typical ordered structure characterized by cells organized in an alveolar structure, with tight pentagonal and hexagonal packing.[3] Crouvisier-Urion et al. have distinguished the cell structure of harvested cork along planes perpendicular to the axial, radial, and tangential directions with respect to the tree.[3] The hexagonal/pentagonal structure of the surface is characteristic of the radial plane, with rectangular cells seen in the cross section (Figure 3e,f) corresponding to the tangential/axial plane.
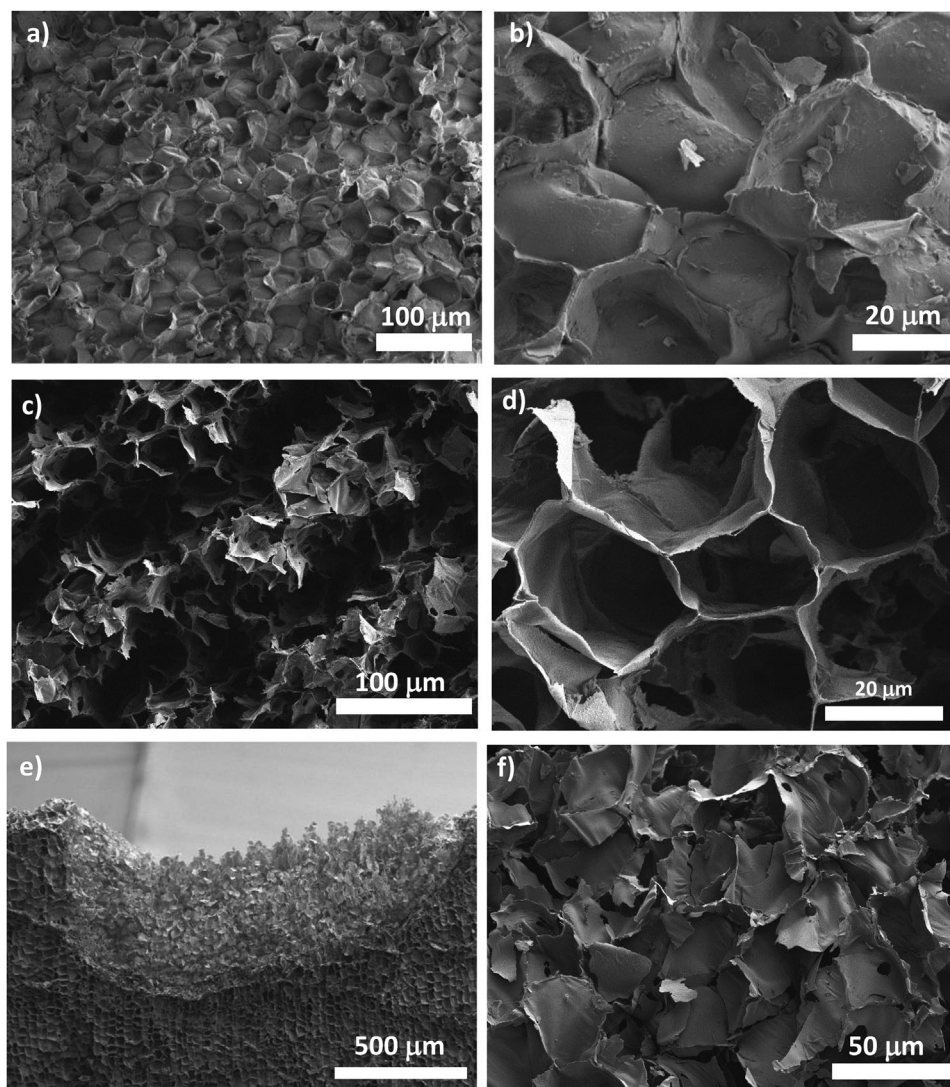
2300026 (3 of 12)

Figure 3. SEM micrographs displaying. a) Low-magnification raw cork surface. b) High-magnification raw cork surface. c) Low-magnification cork-LIG surface. d) High-magnification cork-LIG surface. e) Cross-section of cork-LIG electrode (enhanced contrast). f) High-magnification cross-section cork-LIG.

Upon laser graphitization, low (3c) and high (3d) magnification SEM images show that the original honeycomb structure of the cork was maintained. The cell bases appear ablated, leaving residual long, hollow columns. This is similar to the conversion seen for carbonization of cork at 1000 °C, but in contrast to UV cork-LIG in which cork cells collapsed to leave thin LIG layers.[25,27] The effect of the laser raster movement is evident in Figure 3d. The surface morphology displayed distinctive grooves. The structure differed from the familiar wrinkled, porous structure seen in polyimide LIG (PI-LIG).[8,11] It is known that the morphology of PI-LIG is caused by explosions of trapped gas pockets created by the out-gassing of nitrogen and oxygen during graphitization.[8] In the case of cork-LIG, the underlying porous nature of pristine cork likely allowed for the removal of oxygen without creating pressurized, trapped gas. The cross sectional SEM (Figure 3,e) shows that the cork was graphitized to uneven depths. This is most likely due to the inhomogeneity of the naturally precursor.

The LIG width ranged from 500–680 µm, while the largest recession of the LIG surface from the cork surface was 195 µm. This is very deep for LIG formation, surpassed in literature only by LIG formed on wood (see **Table 1**).

Figure 4a shows a representative Raman spectrum for the cork-LIG material obtained under optimized laser parameters. The spectrum is characterized by three main peaks centered at 1345, 1578, and 2689 cm^{-1} corresponding to the D peak (induced by bent sp^2 carbon bonds and associated with the presence of defects), G peak (corresponding to the E_{2g} vibration mode of graphitic carbon) and 2D peak, respectively.[33,34] The D, G, and 2D peaks were each fitted with Lorentzian peaks with full width at half maximums (FWHM) of 57, 42, and 70 cm^{-1}, respectively. The sharpness of these peaks indicates the high quality of the cork-LIG. The low intensity of the D peak relative to the G peak confirms the low density of defects formed.[35] The high intensity of 2D peak shows the formation of graphene-like carbon

Table 1. Comparison of LIG derived from natural material.

| Material	Laser	Raman [D/G]	Raman [2D/G]	Depth [μm]	R_{sh} [Ω sq^{-1}]	Refs.
Polyimide	IR	0.5		30	23	[8]
Paper	UV (355 nm)				125	[12]
Wood	IR (10.6 μm)	0.8	0.5	800	10	[16]
Watercolor paper	IR	1			40	[30]
Filter paper	IR	1			40	[31]
Chromatography paper	IR	0.5			32	[14]
Chromatography paper	IR	1.28	0.62	10–30	56	[21]
Cellulose nanofibers	IR			70	16 000	[13]
Paper cardboard	IR	0.7		300		[15]
Agglomerated Cork	IR			300	115	[28]
Agglomerated Cork	IR	0.5	0.5	100	10	[32]
Agglomerated Cork	UV		0.37	140	75	[27]
Natural Cork	450 nm	1	0.37		46	[26]
Natural Cork	450 nm	0.8	0.9	500–680	10.8	This work
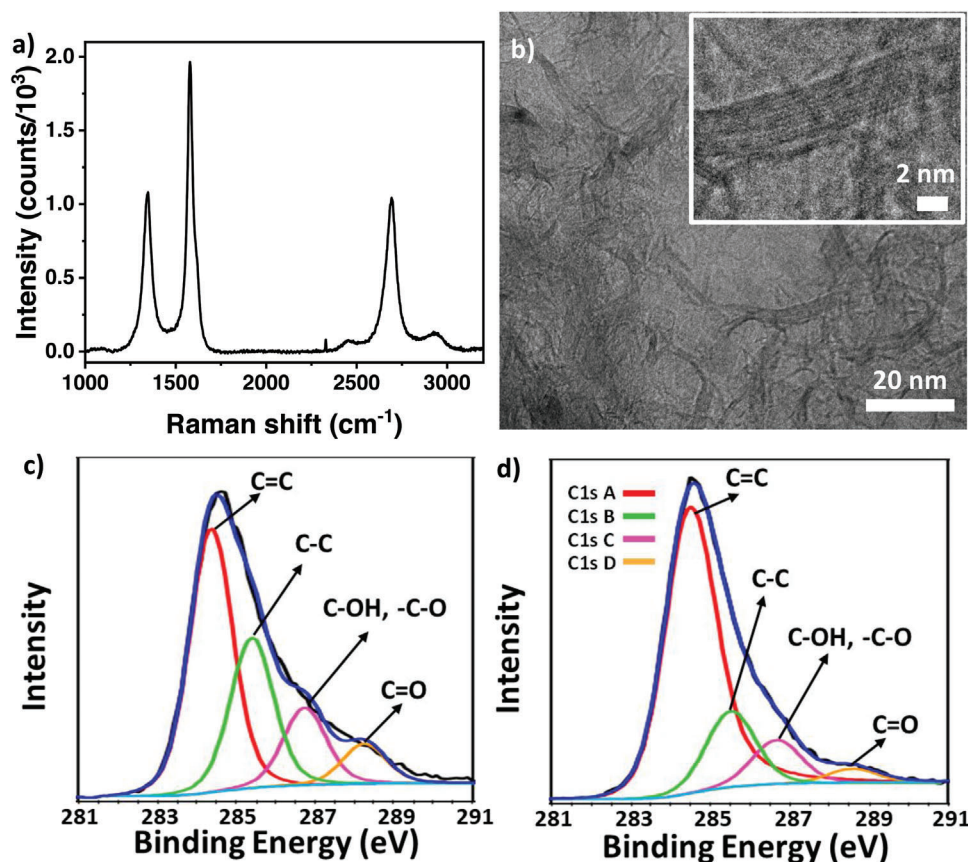
Figure 4. a) Representative Raman spectrum of cork-LIG electrode. b) TEM image of cork-LIG surface. c) C1S XPS spectrum of raw cork. d) C1S XPS spectrum of cork-LIG.

structures. The ratio of integrated intensities I_D/I_G equal to 0.8 confirms the crystalline nature of the ablated surface, whereas the high I_{2D}/I_G of 0.9 indicates a multilayer graphene structure.[36] In accordance with the work of Robertson and Ferrari, this cork-LIG Raman data suggest a material with nanocrystalline graphitic domains in a disordered carbon matrix.[33] This profile is consistent with 2D graphitic structures consisting of randomly stacked graphene layers along the c-axis, already reported for LIG structures obtained by laser writing of polyimide with this 450 nm laser and with high power infrared laser sources.[8,11,35]

**ADVANCED
SCIENCE NEWS**

www.advancedsciencenews.com

**ADVANCED
SENSOR
RESEARCH**

www.advsensorres.com

Table 2. Summary of XPS analysis of raw cork sample, LIG on cork, and reduced cork-LIG.

Peak	Atomic percentages [%]			Assignments
	Cork	Cork-LIG	Activated cork-LIG	
C1s A	42.3	61	78.7	C—C sp^2
C1s B	12.4	8.4	2.1	C—O(H), C—O
C1s C	6.4	2.6		C=O, O—C=O
C1s D	24.1	14.6	10	C—C sp^3
O1s A	9.1	5.3	3.5	C—O
O1s B	2.7	3.8	2.7	O=C—O, H$_2$O
O1s C	1.9	2.9	2.0	O—H
N1s	2			N—C
Total C	85.1	86	90.8	
Total O	13.7	12	8.2	
C1s A/(B+C+D)	0.99	2.38	6.25	
C1s A/O	3.13	5	10	
D parameter [eV]	14.5	14	15	

TEM data (Figure 4b) displays many multilayered graphene domains. The calculated interlayer spacing was 3.47 Å. For bilayer graphene, the figure is 3.4 Å, while for bulk graphite it can vary between 3.34 and 3.69 Å. [37,38] For LIG structures obtained from cork, wood, and PI the average lattice spacing ranged from 3.4–3.5 Å.[8,16,26]

Figure 4c,d shows the deconvoluted C1S X-ray photoelectron spectroscopic (XPS) scans of pristine cork and cork-LIG, respectively. Both spectra are dominated by a large C1s A peak, representing the contribution from C=C bonds. Contributions from other carbon bonds were labeled B (C—C), C (C—OH, —C—O), and D (C=O). **Table 2** shows the summary of atomic percentages found in XPS for pristine cork sheets, cork-LIG, and the electrochemically activated cork-LIG (to be discussed later). The structures were compared in terms of C1s-A atomic %, ratio of A:(B+C+D) peaks in the C1s, total oxygen atomic percentage, ratio of C1s-A:O, and the D parameter. In the pristine cork sample, the C1s-A peak represented an overall atomic percentage of 42.3%, which increased to 61.0% in the cork-LIG material. The large peak observed in the raw cork was ascribed to cork's primary constituents suberin and lignin, both highly aromatic compounds.[39] The increased signal in the laser-treated region was associated to the conversion from cork to LIG, a graphene-like material—in agreement with the Raman data. In particular, the ratio of the A peak with the other carbon components [A/(B+C+D)] indicates the content of C=C carbon (graphite or graphene), whereas the ratio of the A peak with the total oxygen indicates the quality of the laser treatment. As expected, both parameters were greater in the cork-LIG than the untreated cork, indicating a higher content of C=C bonds and a lower content of oxygen. The oxygen content of graphitic structures has also been cited as an indirect method of deducing the density of edge defects, associated with an enhanced chemical and electrochemical reactivity.[40,41] Oxygen groups form and migrate to graphitic edge sites.[42,43] The oxygen content in LIG (12%) can be related to a large exposure of edge planes. The value of the D parameter was 14 eV for the cork-LIG. Values of 13.5–15 eV are typical for graphene, whereas for graphite it is 21.2 eV. The low D value

for the untreated sample is typical for polymers with different C—O bonds.[44] The O1s scans and C KVV scans of all samples are shown in Figure S3 (Supporting Information).

Transmission line method (TLM) measurements are displayed in Figure S4a (Supporting Information). The channel resistance versus track length data averaged from 7 TLM devices is shown. Sheet resistance, R_{SH}, of 10.8 Ω sq^{-1} was calculated by linear regression. This value is as low as has been reported for LIG on natural substrates (see **Table 1**).

The quality of LIG material obtained by graphitization of PI and lignin-rich substrates is compared in Table 1 (Supporting Information). The sheet resistance (R_{sh}) reported here was comparable or lower than the resistance calculated for most fabricated structures and lower than the R_{sh} reported for cork graphitized by UV laser. When comparing with other natural materials, pretreatments should be noted for [12,31] (both sprayed with flame retardant "AntiFlame"),[32] (wax coating),[30] (FeCl3 coating), and [21] (sodium borate pretreatment and wax coating).

2.4. Electrochemical Characterization

The electrochemical properties of the fabricated electrodes were investigated by using the $[Fe(CN)_6]^{3-/4-}$ redox mediator probe. The 3-electrode sensor shown in Figure 1b was used for all measurements. While performing this characterization, drastic changes were observed during 10 min of $[Fe(CN)_6]^{3-/4-}$ cycling. **Figure 5**a shows 50 CV scans taken at 200 mV s^{-1} scan rate on a cork-LIG electrode, with the 1st and 50th scan highlighted. A reduction of ≈4 times was observed in the ΔE_P value, from ≈500 mV for scan 1 to <130 mV for scan 50, as well as an increase in peak current of ≈2.5 times (from 47 μA for cycle 1–119 μA for cycle 50). Figure 5b shows the changes of ΔE_P and I_P observed for 300 CV cycles. The ΔE_P values sharply dropped during the first 50 cycles and showed small fluctuations thereafter. The I_P values sharply increased during the first 50 cycles and contined to increase at a lower rate for susequent cycles. Such changes were ascribed to electrode surface changes. Reduction of surface
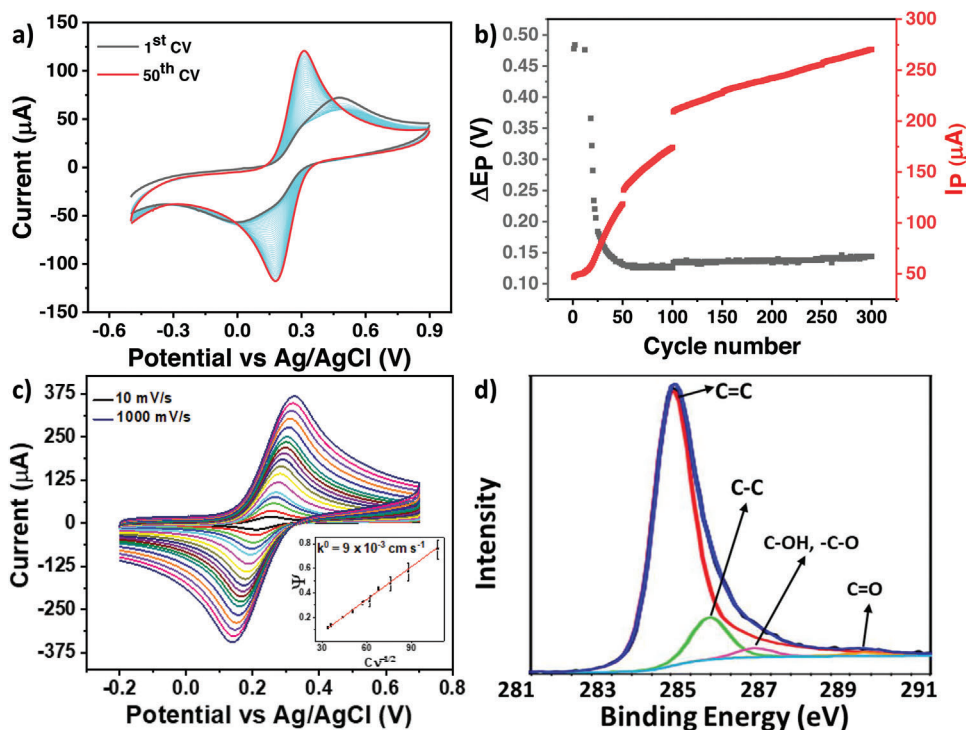
ADVANCED
SCIENCE NEWS
www.advancedsciencenews.com

ADVANCED
SENSOR
RESEARCH
Open Access
www.advsensorres.com

Figure 5. a) 50 CV scans (1st and 50th highlighted) measured on cork-LIG electrodes using $[Fe(CN)_6]^{3-/4-}$ (5 mM, 1 M KCl) at 200 mV s^{-1}. b) Peak separation and current intensities measured for 300 CV cycles. c) CV of $[Fe(CN)_6]^{3-/4-}$ pretreated cork-LIG electrode at varying scan rate from 10 mV s^{-1} to 1 V s^{-1}. Inset: calculation of k^0_{app} for $n = 5$ electrodes. d) C1s XPS spectrum of pre-treated cork-LIG electrode after 10 min $Fe(CN)_6^{3-/4-}$ cycling.

oxygen and oxygenated groups has been reported by cycling LIG electrodes in supporting electrolyte, resulting in enhanced electrochemical properties.[45] In order to decide at what stage of this cycling activation process to stop, CVs at varying scan rates (50–1000 mV s^{-1}) were taken at the 50th and 100th cycle (see details in Figure S5, Supporting Information). The increase of I_P beyond cycle 50 was not accompanied by an equivalent improvement in the kinetic qualities. Therefore, an activation period of 10 min (50 cycles) was deemed sufficient for the electrode to achieve optimal kinetic performance, and satisfactory I_P responses. Also, longer activations times may be associated with electrode degradation as the analyte penetrates the porous material (observed in practice).

An investigation of the electrochemical cycling window showed that the oxygen reduction at ≈-0.6 V, rather than any effect directly related to the redox cycling of $[Fe(CN)_6]^{3-/4-,}$ was the event which allowed for an improved electrochemical performance (see Figures S6 and S7, Supporting Information). A solution of 1 M KCl was used for the activation treatment.

Figure 5c shows a typical set of CV measurements in $Fe(CN)_6^{3-/4-}$ at varying scan rates obtained after the 10 min activation process. Remarkably, even at rapid scan rates of 1 V s^{-1}, ΔE_P values of < 200 mV were maintained. The formal potential ($E_{1/2}$) for $Fe(CN)_6^{3-/4-}$ was found to be 231 mV for the 3-electrode planar system, with standard deviation of 4 mV over 55 measurements. The low deviation indicates the stability of the Ag/AgCl paste RE. Compared with the same redox couple in the same system measured with an external electrode (Figure S2c, Supporting Information), there was a 36 mV potential shift ($E_{1/2}$ = 267 mV). The average ΔE_P calculated at 100 mV s^{-1} scan rate over four elec-

trodes was 90 mV ($\pm$ 4 mV), indicating a quasireversible reaction with fast HET rates.

At low scan rates (< 50 mV s^{-1}) peak separation values below the reversible limit (59 mV for a one electron reaction) were observed for numerous electrodes. These results on a porous electrode suggest that a thin layer mechanism, resulting from electrolyte trapped within the porous network, occurs in parallel with the bulk semi-infinite linear diffusion regime operating at the surface. Indeed, the peak current behavior in the low scan rate region suggested a thin-layer contribution, where the peak current was linear with the scan rate. For semi-infinite linear diffusion, peak currents was proportional to the square root of the scan rate. This was the dominant mechanism at scan rates > 50 mV s^{-1}, and the contribution of the thin layer mechanism did not perturb the expected peak current response. Lyons et al. explained such scan rate dependent behavior by reasoning that high scan rates there is not enough time for diffusion through the pores of the electrode and hence no significant contribution from thin layer behavior; at low scan rates, there is a significant contribution from species diffusing within the electrode structure.[46] These results are summarized in Figure S8 (Supporting Information). The plot of peak anodic and cathodic current versus square root of scan rate, example shown in Figure S9 (Supporting Information) across a wide range of scan rates, displayed excellent linearity, in line with the Randles–Sevcik equation and indicating the dominant semi-infinite linear diffusion regime. Streeter et al. have investigated similar effects on glassy carbon electrodes modified with carbon nanotubes, where analyte can become trapped between nanotubes and exhibit thin layer behavior.[47] They have

Table 3. Electrochemical performance of LIG produced from various precursors and by various lasers using $[Fe(CN)_6]^{3-/4-}$. ΔE_P values quoted at scan rates varying between 50 and 150 mV s^{-1} and at 100 mV s^{-1} for this work.

Material	Laser	ΔE_P [mV]	k^0_{app} [cm s^{-1}]	Refs.
Filter paper	IR (10.6 µm)		7.8×10^{-4}	[31]
Office paper	IR (10.6 µm)	>700	4.08×10^{-4}	[21]
Chromatography paper	IR (10.6 µm)	370	6.85×10^{-4}	[21]
Chitosan	IR (10.6 µm)	290		[18]
Polyimide	Visible (450 nm)	61	1.26×10^{-1}	[11]
Polyimide	UV (405 nm)	86	1.3×10^{-2}	[10]
Cork	Visible (450 nm)	90	9×10^{-3}	This work

warned against interpreting low peak separation values solely in terms of improved catalytic effects or kinetics. The thin-layer mechanism must be taken into account. In the literature on LIG devices, this effect is not commonly investigated. Hence, for a comparison with literature, a value of the heterogeneous electron transfer kinetic constant (k^0_{app}) must be calculated. For this, we have restricted the data used to the high scan rate region (0.1–1 V s^{-1}) where the semi-infinite linear diffusion regime dominates.

From the ΔE_P values, k^0_{app}, was calculated by the Nicholson method (see the Supporting Information for details of calculation).[48] The value calculated for these cork-LIG electrodes was 9×10^{-3} cm s^{-1}. **Table 3** reports the electrochemical characteristics of cork-LIG in comparison with other LIG electrode materials obtained by direct laser writing of sustainable substrates and benchmarked against PI-LIG. The cork-LIG exhibited the lowest ΔE_P of the natural LIGs. The k^0_{app} was one order of magnitude higher than the value calculated for filter paper. In comparison with polyimide LIG electrodes previously obtained in our group with other hobbyist lasers (450 and 405 nm), the cork-LIG displayed comparable ΔE_P but lower HET rate.

XPS analysis was carried out on the pretreated cork-LIG electrode in order to elucidate the mechanism behind the observed electrochemical activation process. Figure 5d shows the deconvoluted C1s XPS spectrum of the pretreated cork-LIG. The C1sA peak dominated the spectrum, as already observed for the pristine cork and the raw cork-LIG samples (see Figure 3c,d and Table 2). However, the atomic percentage assigned to the C1sA peak increased from 61% measured for cork-LIG to 78.7% measured for pretreated cork-LIG, suggesting a large relative increase in C=C bonding following the pretreatment. The ratio of the A peak to other carbon peaks more than doubled and the oxygen content decreased by almost a third. It is clear that the electrochemical treatment was accompanied by a stark improvement in graphene quality. The C1s-B, -C, and -D peaks (see Table 2), which all relate to forms of C—O bonding, were considerably reduced, in line with the electrochemical reduction of surface oxygen. The need for a reduction/activation treatment has been reported for LIG electrodes fabricated from polyimide, and was associated to the impurities of LIG derived from the decomposition process and ambient temperature.[45]

Surface wettability was measured by contact angle. The results of the raw cork, cork-LIG, and electrochemically pretreated cork-LIG are shown in Figure S4b–d (Supporting Information). Both the raw cork and the cork-LIG surfaces were found to be hydrophobic, with contact angles of 124.5° and 107.5°, respectively.

After electrochemical pretreatment of the surface a contact angle of 29° was measured. A more hydrophilic surface is desirable for electrochemical applications, as analyte gaining access to the high surface-area, porous LIG structure would result in enhanced current responses. Because the electrochemical pretreatment resulted in a lowering of the oxygen content, it is understood that the improvement in wettability is due to the removal of surface residues from the lasing process.

2.5. Tyrosine Detection

Tyrosine (Tyr) is a small but important electrochemically active amino acid involved in the regulation of dopamine, adrenaline and thyroid hormones. Although Tyr is a nonessential amino acid, its imbalance has been associated with the development of serious illnesses, including eating disorders, liver diseases, and tyrosinemia.[49–51] Due to its relevance in brain signaling and in the production of stress hormones, it is important to develop rapid, accurate, and low cost methods for monitoring of Tyr levels in biological fluids.

The three-electrode device, after 10 min of pretreatment, was used for Tyr detection without modification. Sodium acetate buffer (ABS), 0.01 M, was chosen as the supporting electrolyte for initial measurements, as the Tyrosine oxidation peak was shifted away from the hydrolysis at ≈1 V (see Figure S10 for details, Supporting Information). **Figure 6**a shows a typical set of square wave voltammetry (SWV) scans for varying Tyr concentrations between 5 and 250 µm. The Tyr peak was centered around 670 mV. Peak current was found to increase linearly with Tyr concentration in the range 5–150 µm, as shown in Figure 6b. From this analysis, the sensitivity of the device was calculated at 8.7×10^{-3} µA µm, with an LOD of 4.8 µm by the $3\sigma/m$ method (see the Supporting Information for calculation). Given that Tyr levels in sweat are known to range from 70 to >200 µm, and in urine from 60 to 130 µm, this is a useful dynamic range.[52] Since Uric acid (UA) is found in most biofluids alongside Tyr, the effect of UA's presence in solution with Tyr was investigated. Figure 6c shows SWV scans of varying concentration Tyr (5–250 µm) in presence of constant UA concentration (50 µm). UA detection was characterized by a peak centered at 300 mV, which did not interfere in the monitoring of Tyr, whose peak remained centered at 670 mV. A linear calibration curve was obtained, as shown in Figure 6d, with sensitivity of 8.2×10^{-3} µA µm^{-1}, in excellent agreement with the value measured in absence of UA. Next,

ADVANCED
SCIENCE NEWS

www.advancedsciencenews.com

ADVANCED
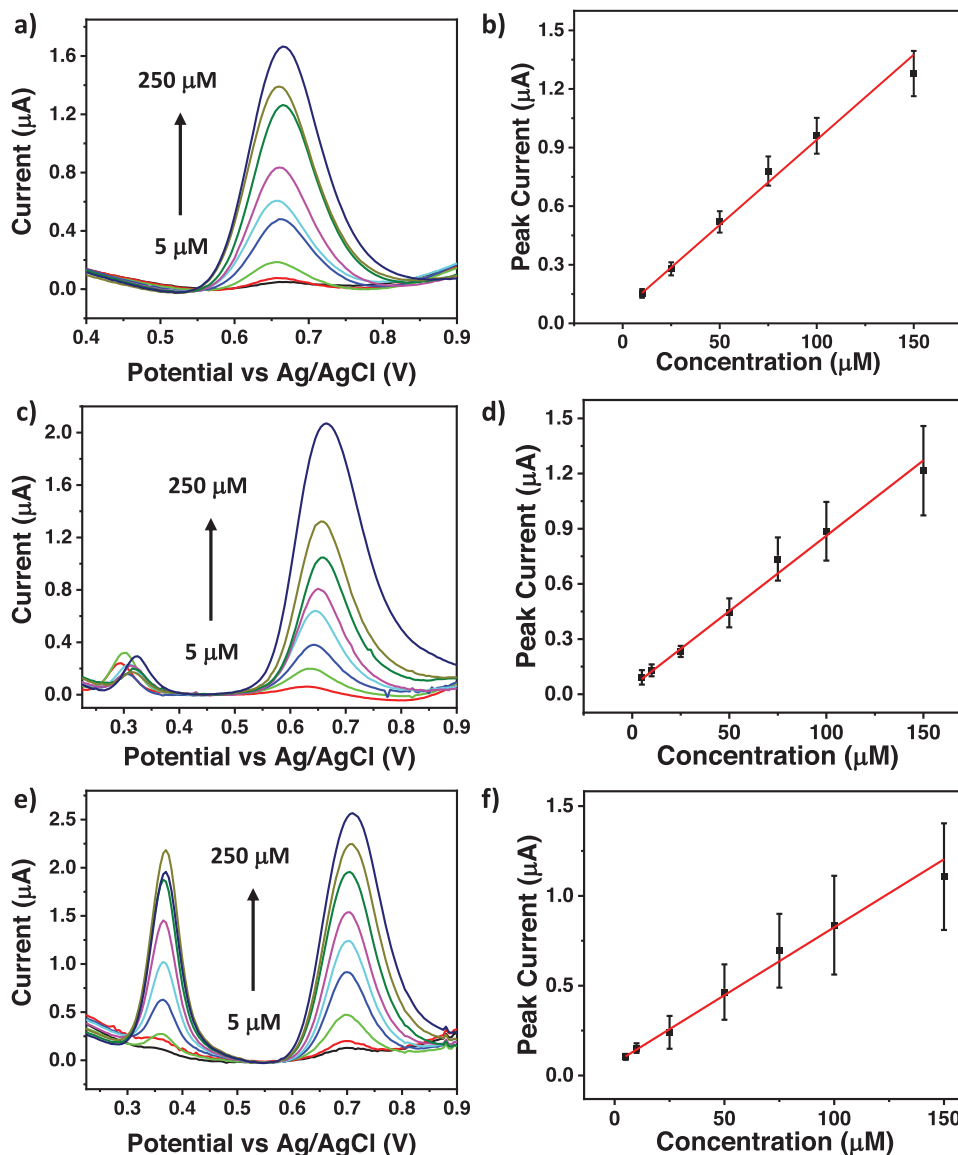SENSOR
RESEARCH
Open Access

www.advsensorres.com

Figure 6. a) Typical set of SWV measurements for various Tyr concentrations. b) Calibration plot. c) Detection of Tyr in the presence of 50 μm UA. d) Linear calibration plot for Tyr in 50 μm UA. e) Simultaneous variation of UA and Tyr concentration. f) Linear calibration plot for Tyr. $n = 3$ devices for all calibrations.

SWQ scans were taken of varying Tyr and UA concentrations. Figure 6e shows the increase in intensity for the peak centered at as UA concentrations varied between 5 and 250 μm. The scans also showed the parallel increase in peak intensity for Tyr concentrations between 5 and 250 μm. A linear calibration (Figure 6f) was obtained for Tyr, showing the reaction of UA to not be a competing or interfering reaction.

The selectivity of the cork-LIG electrode toward Tyr was evaluated by taking SWV scan of Tyr in the presence of UA, Urea, Glucose, dopamine (DA), and ascorbic acid (AA) at biologically relevant concentration levels (50 μm UA, 10 mm Urea, 150 μm Glucose, 25 μm DA, 50 μm AA).[52] **Figure 7**a shows that DA, UA, and Tyr displayed well separated and well-defined peaks, centered at 180, 330, and 670 mV, respectively. No peaks for urea, glucose, or AA appeared, indicating no electrochemical reaction

with the electrode. The Tyr peak is in line with the previous calibrations. Interesting too is the intense DA peak at low concentration. An individual calibration for DA was performed, and a LOD of 1.1 μm (see Figure S11, Supporting Information) is obtained. This value is lower than that reported for LIG produced from commercial polyimide.[11] The cork-LIG electrochemical platform allowed simultaneous detection of DA, UA, and Tyr within a narrow potential window, owing to the fast electron transfer kinetics of the material.

Finally, the applicability of the cork-LIG electrochemical sensor for the determination of Tyr was tested in artificial sweat. The matrix of the artificial sweat was prepared with slight changes according to literature.[53,54] Artificial sweat contained NaCl (20 g L^{-1}), NH$_4$Cl (17.5 g L^{-1}), lactic acid (15 g L^{-1}), acetic acid (5 g L^{-1}), ascorbic acid (10 μm), uric acid (60 μm), and urea (10 mm).
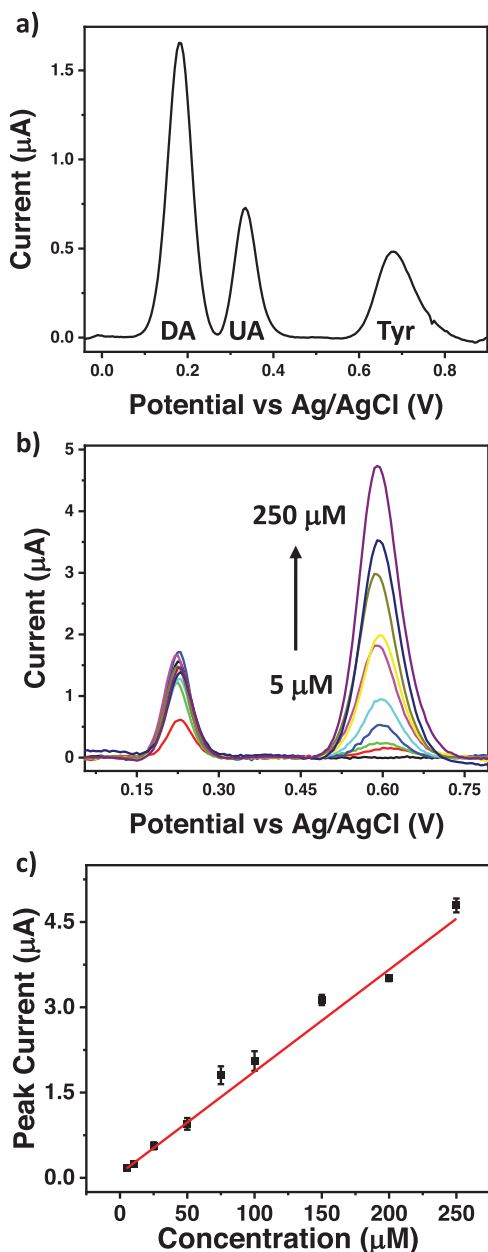
300 μm), the proposed electrochemical sensor could be an excellent candidate for the development of both disposable and wearable environmentally friendly diagnostic devices. **Table 4** compares the Tyr detection of the cork-LIG electrode with other published electrochemical platforms. The reported LOD of 3.75 μm is comparable with the LODs reported for PI-LIG, showing that environmentally friendly substrates can be exploited as precursors to high-quality LIG electrochemical sensors.

3. Conclusions

Novel electrochemical sensors were fabricated by direct laser writing of natural cork from Quercus suber L. The cork-LIG structures displayed a porous, 3D, high surface area morphology, suitable for electrochemical applications. Three terminal electrode sensors were fabricated in less than 10 min, using cork-LIG as working and counter electrode and Ag/AgCl paste as reference electrode. Following a 10 min electrochemical activation process in $[Fe(CN)_6]^{3-/4-}$, the cork-LIG electrodes displayed an average ΔE_P of 90 mV at a scan rate of 100 mV s^{-1}, close to the ideal value for a reversible reaction.[61] The HET kinetics were found to be one order of magnitude higher than other LIG electrodes obtained from wood and/or lignin rich natural substrates. The electrochemical sensors showed excellent sensing performance. Dopamine was detected with an LOD of 1.1 μm. Sensitive detection of Tyr in an artificial sweat solution was achieved with LOD of 3.75 μm. Here we have presented a natural material, entirely renewable, recyclable, whose electrical and electrochemical properties rival those of the highest quality LIG. This is exemplified by the simultaneous detection of DA, UA, and Tyr in a narrow potential window, and the sensitive detection in sweat. We can consider the Tyr detection and characterization a showcase of the capabilities of a new and exciting form of LIG sensor. A wide range of sensing applications are made possible by the rapid electron transfer rates at the cork-LIG electrode. This study shows the suitability of cork as natural and abundant precursor material for the realization of next generation green electronics.

4. Experimental Section

Materials: Natural cork sheets with dimensions 40×60 mm with thickness 2 mm (see Figure S1a, Supporting Information) were purchased from Alomejor and used without further treatment. L-Tyrosine, dopamine hydrochloride, uric acid, L-ascorbic acid, urea and D-glucose were purchased from Merck and used without further purification. Sodium Acetate Buffer (ABS) was purchased from Merck at 3 M and diluted to 0.01 M for experiments. Ferrocyanide ($[Fe(CN)_6]^{4-}$) was prepared from $K_4Fe(CN)_6$ (Merck). All solutions were prepared using deionized Milli-Q water (resistivity 18.2 MΩ cm).

Electrode Fabrication: Cork-LIG electrodes were fabricated with a KKmoon Compact Automatic Desktop Laser Engraving Machine equipped with a laser with 3 W power and illumination wavelength of 450 nm. Electrode structures were designed in Microsoft PowerPoint and transferred to the laser engraving software, which wrote them to the cork substrate by raster scanning of the laser beam. Laser power (LP, % of 3 W) and depth adjustment (DA—a KKmoon parameter related to laser dwell time) were adjusted in the laser engraving software. Ag/AgCl paste was purchased from Merck and applied directly to the cork. Conductive silver paint (Merck) was applied to the device for electrically contacting the electrodes to the potentiostat.

Figure 7. a) Detection of 50 μm Tyr in the presence of 50 μm Uric Acid, 10 mM Urea, 150 μm Glucose, 25 μm DA, 50 μm AA. b) SWV plots of varying Tyr concentration in artificial sweat solution. c) Linear calibration plot of b) for n = 3 devices.

The pH was adjusted to 8.1 using KOH, to shift the Tyr peak to a more negative potential, so that hydrolysis at 1 V does not interfere with the measurement.[53] The current responses of the cork-LIG electrochemical sensor were recorded for different Tyr concentrations in artificial sweat, as shown in Figure 7b. Linear calibration was achieved from 5 to 250 μm. Comparing the slopes of both calibration curves of the Tyr sensor in ABS (8.7 A M^{-1}) and artificial sweat (1.8×10^{-2} A M^{-1}), more sensitive detection was achieved in the sweat solution. The LOD in the sweat solution was 3.75 μm. Considering the normal Tyr level in sweat (60–

Table 4. Tyr detection by different electrode materials.

Material	LOD [M]	Sensitivity	Refs.
PI-LIG	1.5×10^{-6}		[55]
PI-LIG	3.6×10^{-6}	$0.61\ \mu\text{m cm}^{-2}$	[56]
rGO–Cu modified pencil graphite	1×10^{-7}	$0.4\ \mu\text{A ppm}^{-1}\ \text{mm}^{-2}$	[57]
GR/Au NPs/GCE	47×10^{-9}		[58]
rGO/ABPE	0.06×10^{-6}	$3.314\ \mu\text{A}\ \mu\text{m}^{-1}\ \text{cm}^{-2}$	[59]
Egr/GC	1.81×10^{-6}	$1.24 \times 10^{-2}\ \text{A M}^{-1}$	[60]
Cork-LIG	3.75×10^{-6}	$1.8 \times 10^{-2}\ \text{A M}^{-1}$	This work

Characterization: Graphitic carbon electrodes were morphologically characterized by a cold-cathode field-emission SEM (JSM-7500F, JEOL UK Ltd.) operating at 5 kV acceleration voltage. Bright field transmission electron microscopy (TEM) analysis was performed by means of a FEI Tecnai G12 Spirit Twin (LaB6 source) at 120 kV acceleration voltage. TEM images were collected on a FEI Eagle 4 k CCD camera. White light optical microscopy images were acquired with a Zeiss Stemi 508 Microscope interfaced to a Zeiss Axiocam 208 color microscope camera. Raman investigation was performed with Horiba-XPlora equipped with a 532 nm laser (70 mW at sample). Spectra were acquired at a laser power of 10% and 30 s acquisition time. XPS measurements were acquired at room temperature by using an Escalab 250Xi (Thermo Fisher Scientific, UK) spectrometer, equipped with a monochromatic Al Kα excitation source, electron and ion flood guns for charge neutralization and a 6-channeltron detection system. The photoemission spectra were collected at 20 eV pass energy, and the diameter of analyzed area was about 1 mm. The XPS core level spectra of C1s and N1s were analyzed using a fitting routine, where each spectrum was decomposed into a series of individual mixed Gaussian–Lorentzian peaks following a Shirley background subtraction. Surface wettability was measured by a Dataphysics OCA 20 Wetting angle system in air at ambient temperature by dropping distilled water droplets (1 mm diameter) on the surfaces. The average contact angle value was acquired by measuring at three to six different positions per sample.

Two-terminal current–voltage measurements (± 1 V, 20 mV step) were obtained under ambient conditions on TLM structures using an Wentworth PML 8000 probe station and Agilent E4980A parameter analyzer. Track resistance values for varying channel lengths were calculated from linear fits of I–V plots. Plots of track resistance versus channel length were used to calculate sheet resistance (R_{SH}) and contact resistance (R_{CT}).

Electrochemical Analysis: Cyclic voltammetry (CV) and SWV electrochemical measurements were performed with a CHI760 bi-potentiostat. The parameters for the SWV measurements were: 0.005 V increment; 0.025 V amplitude; 5 Hz frequency. Cork-LIG structures, produced at the same laser settings, were used as a working (WE) and counter (CE) electrode. An acrylic based nail varnish was used to delimit the WE area, improving the reproducibility of the active area. Ag/AgCl paste, applied directly to the cork, was used as a reference electrode. For the initial electrochemical optimization, an external Ag/AgCl RE and a Pt wire CE were used. The device was assembled in a Teflon cell with a circular area of 8 mm diameter exposed to the electrolyte. The electrochemical cell setup is shown in Figure S1b (Supporting Information). Heterogeneous electron transfer (HET) rate constants (k^0_{app}) were determined from the anodic/cathodic peak separation using the method of Nicholson[48] by assuming transfer coefficient $\alpha = 0.5$ and using the following diffusion coefficients: $[Fe(CN)_6]^{4-/3-}$ $D_0 = 7.26 \times 10^{-6}\ \text{cm}^2\ \text{s}^{-1}$, $D_R = 6.67 \times 10^{-6}\ \text{cm}^2\ \text{s}^{-1}$.[62]

Electrochemical Pretreatment Activation: Prior electrochemical analysis cork-LIG electrodes were cycled in 1 M KCl for 50 cyclic voltammetry cycles (10 min) from -0.7 to 0.9 V at 200 mV s^{-1}. The reduction of surface oxygen close to -0.5 V was vital for achieving an enhanced electrode performance. A single wide scan was performed prior to the cycling, to ensure that the oxygen reduction event was captured within the -0.7–0.9 V electrochemical window in the case of an initial overpotential.

Supporting Information

Supporting Information is available from the Wiley Online Library or from the author.

Conflict of Interest

The authors declare no conflict of interest.

Author Contributions

E.V., C.S., M.S., C.L., G.G.: formal analysis, investigation; A.J.Q.: editing, review; M.L.: conceptualization; funding acquision, writing; D.L.: funding acquisition, conceptualization, writing.

Data Availability Statement

The data that support the findings of this study are available from the corresponding author upon reasonable request.

[1] S. P. Silva, M. A. Sabino, E. M. Fernandes, V. M. Correlo, L. F. Boesel, R. L. Reis, *Int. Mater. Rev.* **2005**, *50*, 345.

[2] R. H. White, *Wood Fiber Sci.* **1987**, *19*, 446.

[3] K. Crouvisier-Urion, J. Chanut, A. Lagorce, P. Winckler, Z. Wang, P. Verboven, B. Nicolai, J. Lherminier, E. Ferret, R. D. Gougeon, J. P. Bellat, T. Karbowiak, *Sci. Rep.* **2019**, *9*, 19682.

[4] A. P. Duarte, J. C. Bordado, *Front. Mater.* **2015**, *2*, https://doi.org/10.3389/fmats.2015.00002.

[5] K. Griffiths, C. Dale, J. Hedley, M. D. Kowal, R. B. Kaner, N. Keegan, *Nanoscale* **2014**, *6*, 13613.

[6] V. Strong, S. Dubin, M. F. El-Kady, A. Lech, Y. Wang, B. H. Weiller, R. B. Kaner, *ACS Nano* **2012**, *6*, 1395.

[7] R. Ye, D. K. James, J. M. Tour, *Acc. Chem. Res.* **2018**, *51*, 1609.

[8] J. Lin, Z. Peng, Y. Liu, F. Ruiz-Zepeda, R. Ye, E. L. Samuel, M. J. Yacaman, B. I. Yakobson, J. M. Tour, *Nat. Commun.* **2014**, *5*, 5714.

[9] P. Nayak, N. Kurra, C. Xia, H. N. Alshareef, *Adv. Electron. Mater.* **2016**, *2*, 1600185.

[10] M. Burke, C. Larrigy, E. Vaughan, G. Paterakis, L. Sygellou, A. J. Quinn, G. Herzog, C. Galiotis, D. Iacopino, *ACS Omega* **2020**, *5*, 1540.

[11] E. Vaughan, C. Larrigy, M. Burke, L. Sygellou, A. J. Quinn, C. Galiotis, D. Iacopino, *ACS Appl. Electron. Mater.* **2020**, *2*, 3279.

[12] B. Kulyk, B. F. R. Silva, A. F. Carvalho, P. Barbosa, A. V. Girão, J. Deuermeier, A. J. S. Fernandes, F. M. L. Figueiredo, E. Fortunato, F. M. Costa, *Adv. Mater. Technol.* **2022**, *7*, 2101311.

[13] S. Lee, S. Jeon, *ACS Sustainable Chem. Eng.* **2019**, *7*, 2270.

[14] B. Kulyk, B. F. R. Silva, A. F. Carvalho, S. Silvestre, A. J. S. Fernandes, R. Martins, E. Fortunato, F. M. Costa, *ACS Appl. Mater. Interfaces* **2021**, *13*, 10210.

[15] W. R. de Araujo, C. M. R. Frasson, W. A. Ameku, J. R. Silva, L. Angnes, T. R. L. C. Paixão, *Angew. Chem., Int. Ed.* **2017**, *56*, 15113.

[16] R. Ye, Y. Chyan, J. Zhang, Y. Li, X. Han, C. Kittrell, J. M. Tour, *Adv. Mater.* **2017**, *29*, 1702211.

[17] P. I. C. Claro, T. Pinheiro, S. L. Silvestre, A. C. Marques, J. Coelho, J. M. Marconcini, E. Fortunato, L. H. C. Mattoso, R. Martins, *Appl. Phys. Rev.* **2022**, *9*, 041305.

[18] C. Larrigy, M. Burke, A. Imbrogno, E. Vaughan, C. Santillo, M. Lavorgna, L. Sygellou, G. Paterakis, C. Galiotis, D. Iacopino, A. J. Quinn, *Adv. Mater. Technol.* **2023**, *8*, 2201228.

[19] H. Awasthi, U. S. Jayapiriya, H. Renuka, M. D. Wagh, A. Kothuru, A. K. Srivastava, S. Goel, *IEEE Sens. J.* **2022**, https://doi.org/10.1109/JSEN.2022.3170538.

[20] Y. Chyan, R. Ye, Y. Li, S. P. Singh, C. J. Arnusch, J. M. Tour, *ACS Nano* **2018**, *12*, 2176.

[21] T. Pinheiro, S. Silvestre, J. Coelho, A. C. Marques, R. Martins, M. G. F. Sales, E. Fortunato, *Adv. Mater. Interfaces* **2021**, *8*, 2101502.

[22] H. Park, M. Kim, B. G. Kim, Y. H. Kim, *ACS Appl. Nano Mater.* **2020**, *3*, 6899.

[23] C. H. Dreimol, H. Guo, M. Ritter, T. Keplinger, Y. Ding, R. Günther, E. Poloni, I. Burgert, G. Panzarasa, *Nat. Commun.* **2022**, *13*, 3680.

[24] T.-S. D. Le, Y. A. Lee, H. K. Nam, K. Y. Jang, D. Yang, B. Kim, K. Yim, S.-W. Kim, H. Yoon, Y.-J. Kim, *Adv. Funct. Mater.* **2022**, *32*, 2107768.

[25] J. S. Lee, J. Lee, J. M. Yoo, T. Kim, Y. H. Kim, *ACS Appl. Mater. Interfaces* **2017**, *9*, 43959.

[26] A. Imbrogno, J. Islam, C. Santillo, R. Castaldo, L. Sygellou, C. Larrigy, R. Murray, E. Vaughan, M. K. Hoque, A. J. Quinn, D. Iacopino, *ACS Appl. Electron. Mater.* **2022**, *4*, 1541.

[27] A. F. Carvalho, A. J. S. Fernandes, R. Martins, E. Fortunato, F. M. Costa, *Adv. Mater. Technol.* **2020**, *5*, 2000630.

[28] M. G. Stanford, J. T. Li, Y. Chyan, Z. Wang, W. Wang, J. M. Tour, *ACS Nano* **2019**, *13*, 7166.

[29] R. Murray, M. Burke, D. Iacopino, A. J. Quinn, *ACS Omega* **2021**, *6*, 16736.

[30] Y. Chyan, J. Cohen, W. Wang, C. Zhang, J. M. Tour, *Graphene Art. ACS Appl. Nano Mater.* **2019**, *2*, 3007.

[31] B. Kulyk, S. O. Pereira, A. J. S. Fernandes, E. Fortunato, F. M. Costa, N. F. Santos, *Carbon* **2022**, *197*, 253.

[32] S. L. Silvestre, T. Pinheiro, A. C. Marques, J. Deuermeier, J. Coelho, R. Martins, L. Pereira, E. Fortunato, *Flexible Printed Electron.* **2022**, *7*, 035021.

[33] A. C. Ferrari, J. Robertson, *Phys. Rev. B* **2000**, *61*, 14095.

[34] A. C. Ferrari, D. M. Basko, *Nat. Nanotechnol.* **2013**, *8*, 235.

[35] P. Lespade, R. Al-Jishi, M. S. Dresselhaus, *Carbon* **1982**, *20*, 427.

[36] V. T. Nguyen, H. D. Le, V. C. Nguyen, T. T. Tam Ngo, D. Q. Le, X. N. Nguyen, N. M. Phan, *Adv. Nat. Sci. Nanosci. Nanotechnol.* **2013**, *4*, 035012.

[37] A. M. Popov, I. V. Lebedeva, A. A. Knizhnik, Y. E. Lozovik, B. V. Potapkin, N. A. Poklonski, A. I. Siahlo, S. A. Vyrko, *J. Chem. Phys.* **2013**, *139*, 154705.

[38] G. Çakmak, T. Öztürk, *Diamond Relat. Mater.* **2019**, *96*, 134.

[39] H. Periera, *BioResources* **2013**, *8*, 2246.

[40] C. E. Banks, T. J. Davies, G. G. Wildgoose, R. G. Compton, *Chem. Commun.* **2005**, 829. https://doi.org/10.3389/fmats.2015.00002

[41] N. F. Santos, S. O. Pereira, A. Moreira, A. V. Girão, A. F. Carvalho, A. J. S. Fernandes, F. M. Costa, *Adv. Mater. Technol.* **2021**, *6*, 2100007.

[42] R. T. Yang, C. Wong, *Science* **1981**, *214*, 437.

[43] G. G. Wildgoose, P. Abiman, R. G. Compton, *J. Mater. Chem.* **2009**, *19*, 4875.

[44] S. Kaciulis, A. Mezzi, S. K. Balijepalli, M. Lavorgna, H. S. Xia, *Thin Solid Films* **2015**, *581*, 80.

[45] F. Vivaldi, A. Dallinger, N. Poma, A. Bonini, D. Biagini, P. Salvo, F. Borghi, A. Tavanti, F. Greco, F. Di Francesco, *APL Bioeng.* **2022**, *6*, 036104.

[46] G. P Keeley, M. E. G. Lyons, *Int. J. Electrochem. Sci.* **2009**, *4*, 794.

[47] I. Streeter, G. G. Wildgoose, L. Shao, R. G. Compton, *Sens. Actuators, B* **2008**, *133*, 462.

[48] R. S. Nicholson, *Anal. Chem.* **1965**, *37*, 1351.

[49] G. D'Andrea, R. Ostuzzi, A. Bolner, F. Franceschini, F. Musco, F. d'Onofrio, D. Colavito, *Neurol. Sci.* **2008**, *29*, 88.

[50] R. J. Levine, H. O. Conn, *J. Clin. Invest.* **1967**, *46*, 2012.

[51] D. González-Lamuño, P. Sánchez-Pintos, F. Andrade, M. L. Couce, L. Aldámiz-Echevarría, *Orphanet. J. Rare Dis.* **2021**, *16*, 256.

[52] C. J. Harvey, R. F. LeBouf, A. B. Stefaniak, *Toxicol. In Vitro* **2010**, *24*, 1790.

[53] C. Callewaert, B. Buysschaert, E. Vossen, V. Fievez, T. Van de Wiele, N. Boon, *J. Microbiol. Methods* **2014**, *103*, 6.

[54] T. Kilic, V. Brunner, L. Audoly, S. Carrara, "Smart e-Patch for drugs monitoring in schizophrenia," 2016 IEEE International Conference on Electronics, Circuits and Systems (ICECS), Monte Carlo, Monaco, Italy **2016**.

[55] T. A. Matias, R. G. Rocha, L. V. Faria, E. M. Richter, R. A. A. Munoz, *ChemElectroChem* **2022**, *9*, e202200339.

[56] Y. Yang, Y. Song, X. Bo, J. Min, O. S. Pak, L. Zhu, M. Wang, J. Tu, A. Kogan, H. Zhang, T. K. Hsiai, Z. Li, W. Gao, *Nat. Biotechnol.* **2020**, *38*, 217.

[57] C. Kavitha, K. Bramhaiah, N. S. John, *RSC Adv.* **2020**, *10*, 22871.

[58] M. Liu, J. Lao, H. Wang, Z. Xu, J. Li, L. Wen, Z. Yin, C. Luo, H. Peng, *Russ. J. Electrochem.* **2021**, *57*, 41.

[59] P. Deng, J. Xiao, J. Feng, Y. Tian, Y. Wu, J. Li, Q. He, *Microchem. J.* **2021**, *165*, 106106.

[60] C. Varodi, F. Pogăcean, M. Coroş, A. Ciorîţă, S. Pruneanu, *Sensors* **2022**, *22*, 3606.

[61] A. J. Bard, L. R. Faulkner, H. S. White *Electrochemical Methods: Fundamentals and Applications*, 3rd ed., Wiley, New York **2001**.

[62] S. J. Konopka, B. McDuffie, *Anal. Chem.* **1970**, *42*, 1741.